Available online at www.sciencedirect.com
SCIENCE DIRECT®
International Journal of Heat and Mass Transfer 48 (2005) 1572–1582
International Journal of HEAT and MASS TRANSFER
www.elsevier.com/locate/ijhmt

# Phase change phenomena in silicon microchannels

Lian Zhang *, Evelyn N. Wang, Kenneth E. Goodson, Thomas W. Kenny

*Department of Mechanical Engineering, Stanford, CA 94305-4021, USA*

Received 26 February 2004; received in revised form 6 September 2004
Available online 22 December 2004

**Abstract**

Understanding the boiling process and two-phase flow behavior in microchannels is the key to developing microchannel heat sinks for high-power microprocessors. We conducted experiments in micromachined silicon channels with a range of 27–171 μm hydraulic diameters and varying surface roughnesses. Bubble nucleation, flow patterns, wall temperature, as well as transient pressure fluctuations were recorded and analyzed. We observed both typical nucleate boiling and eruption boiling with large amounts of wall superheat in these channels, and recorded up to 138 kPa transient pressure fluctuations due to bubble nucleation. We found the boiling mechanism is strongly dependent on the wall surface roughness, and we explained the boiling mechanism in sub-150 μm diameter channels with Hsu's model.


## 1. Introduction

In accordance with Moore's Law [1], the number of transistors integrated on Intel microprocessors has increased from $3.1 \times 10^6$ (Pentium, 1993) to $9.5 \times 10^6$ (Pentium III, 1999) to $178 \times 10^6$ (Pentium 4, 800 MHz, 2004) in the past decade [2]. The continual increase in the integration density causes a rapid rise in power generation from microprocessors. With 82 W of heat generation by a Pentium 4 processor, the noise produced by the cooling fan is approaching the acceptable limits for consumers. According to ITRS (International Technology Roadmap for Semiconductor), the heat dissipation from a single cost-performance chip is expected to exceed 100 W by the year 2006 [3]; however the chip temperature must be maintained in the approximate range of 80–100 °C for proper functionality and reliability. By that time, air cooling will no longer satisfy the needs of these high-power chips. Scientists and researchers have long been pursuing solutions for high-power chip thermal management. Since Tuckerman and Pease [4] proposed the idea of liquid cooling with microchannels in 1981, microchannel heat sinks have been considered one of the most promising cooling devices for future high-power chips [5]. The latest idea is to directly attach a microchannel heat sink to the back side of the microprocessor while a coolant is pumped into the channels [6]. The heat generated by the chip is absorbed through the liquid-vapor phase change and is carried by the vapor into a condensing chamber. The vapor condenses and is re-circulated back into the microchannel heat sink. Taking advantage of the latent heat associated with phase change, the heat absorption is much more efficient than that of a single-phase liquid. The recent development of electroosmotic pumps even allows a miniature closed-loop cooling system [7].

* Corresponding author. Present address: Molecular Nanosystems, 977 Commercial Street, Palo Alto, CA 94303, USA.
*E-mail address:* lian@stanfordalumni.org (L. Zhang).

0017-9310/$ - see front matter © 2004 Elsevier Ltd. All rights reserved.
doi:10.1016/j.ijheatmasstransfer.2004.09.048

**Nomenclature**

| | |
|---|---|
| $A$ | Cross sectional are a of a microchannel |
| $c_p$ | specific heat |
| $D_H$ | hydraulic diameter of a microchannel, $D_H = 4A/P_w$ |
| $h_{fg}$ | latent heat |
| $\dot{m}$ | liquid mass flow rate |
| $P_w$ | Wetted perimeter of a microchannel |
| $q$ | heat rate |
| $q^*$ | dimensionless heat rate |
| $r_c$, | cavity radius of an effective nucleation site |
| $T_0$ | liquid entrance temperature |
| $T_\infty$ | bulk liquid temperature |
| $T_{sat}$ | liquid saturation temperature |
| $T_w$ | wall temperature |
| $\Delta T_{sup}$ | wall superheat |
| $v_l$ | specific volume of the liquid at saturation temperature |
| $v_v$ | specific volume of the vapor at saturation temperature |

*Greek symbols*

| | |
|---|---|
| $\delta$ | thermal boundary layer thickness |
| $\sigma$ | liquid surface tension |

However, the phase change phenomena in microchannels are relatively poorly understood due to the lack of experimental studies, especially the visualization of the two-phase flow conditions. Jiang et al. [8] studied water-vapor phase change in 26 and 53 μm V-shaped silicon microchannels. They observed bubble nucleation in large manifolds at the entrance to the microchannels. Steinke and Kandlikar [9] examined flow boiling patterns in 207 μm diameter channels machined into copper plates. They suggested conventional flow boiling patterns also occur in these channels, such as nucleation, bubbly flow, counter flow, churn flow, and dry-out. Peng et al. [10] conducted phase change experiments in $0.6 \times 0.7$ mm stainless steel channels. They reported that the heat transfer in the single-phase regime was prolonged, and fully developed boiling seemed to appear suddenly at unusually high heat fluxes without nucleation or partial boiling process. Kenning and Yan [11] designed a single vertical channel with $2 \times 1$ mm cross section and 248 mm length. They recorded bubble growth in the channel and detected pressure pulses caused by the acceleration of liquid slugs resulting from confined bubble growth. Peles et al. [12,13] studied the phase change in 50–200 μm diameter silicon channels. They recorded an oscillating evaporation front between the vapor bubble and the liquid and associated pressure fluctuations. They also proposed that explosive boiling might occur at small Peclet numbers, which leads to fine bubble growth, blockage of the channel, and vapor explosion. In the previous research, bubble nucleation has been visualized in both larger than 1 mm diameter channels and large areas such as manifolds in microchannel test devices. However, the much smaller channels, where opposite observations and a unique "explosive boiling" are more often reported, are of more interest to the study of microchannel heat sinks. In this paper, we focus on how the phase change occurs and how the two-phase flow develops in micromachined silicon channels with less than 150 μm hydraulic diameters.

## 2. Experimental system

Thermally isolating the microchannel is important to minimize experimental uncertainties. In our previous study, we have successfully carried out heat transfer experiments in a single microchannel fabricated on a thermally isolated silicon beam [14]. On the basis of this concept, we designed single-channel devices with 5–10 Ω/°C temperature sensitivity and 0–10 W heating capability for both steady state and transient measurements. The test system allows simultaneous heat flux control, wall temperature measurement, pressure drop measurement, as well as optical imaging of the two-phase flow conditions.

### 2.1. Instrumented microchannels

As shown in Fig. 1, the $6.5 \times 2$ cm microchannel chip has two mounting pads and a $2 \times 0.2$ cm freestanding beam. On each device, a single rectangular microchannel with inlet and outlet reservoirs is micromachined into the narrow beam. The freestanding beam and the two large reservoirs provide thermal isolation to the heated test channel. The microchannels are 2 cm long, with a hydraulic diameter in the range of 27–171 μm. The channels are fabricated with deep reactive ion etching (DRIE) on the front side of the substrate, with seven doped silicon temperature sensors and aluminum heaters on the back side. Transparent glass cover slides are used to seal the channels, allowing high-speed photography of the internal flow conditions. The design parameters of the device are listed in Table 1.

### 2.2. Experimental setup

Fig. 2 shows the schematic of the experimental setup. The microchannel test device is mounted to a fixture with internal flow channels and directors. The heaters and temperature sensors are connected through a

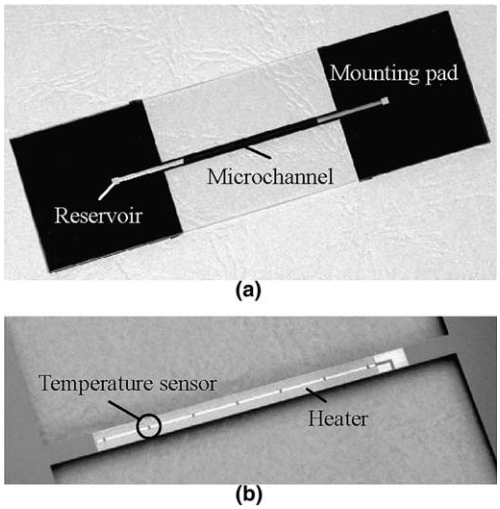


Fig. 1. Microchannels with integrated heaters and temperature sensors. (a) Front side of the microchannel chip with the channel, inlet and outlet reservoirs. (b) Silicon temperature sensors and aluminum heater on the back side.

surface mounting board attached to the device [14]. Deionized (DI) water is pumped into the channel with a constant flow rate syringe pump. By applying a voltage to the on-chip aluminum heater, the microchannel is uniformly heated. The channel wall temperatures are measured through the resistance change of doped silicon temperature sensors, which are evenly distributed along the channel in seven locations. The temperature sensors are 300–350 μm away from the liquid-channel interface and the temperature gradient in the bottom wall is approximately 0.3 °C with the maximum power used in our experiments. The temperature-resistance correlation for each temperature sensor is calibrated before experiments. These temperature sensors have 5–10 Ω/°C temperature sensitivity in the range of 20–150 °C, with ±0.5 °C accuracy. In addition, an MSP-400 pressure transducer is used to measure the global pressure drop along the channel. A SONY 2735 CCD camera (30 frames/s, 1/100,000 s maximum shutter speed) records the two-phase flow conditions simultaneously. The heating power, channel wall temperature, and the pressure signals are collected and recorded with a 16-bit A/D system.

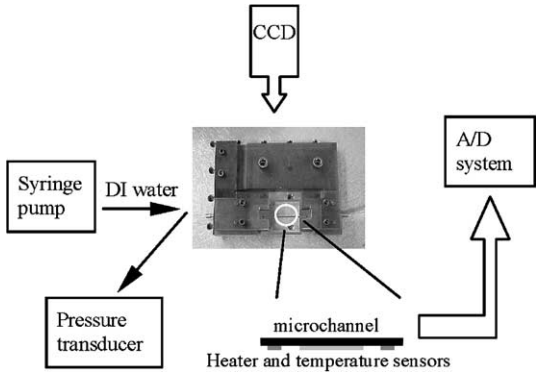


Fig. 2. Schematic of experimental setup.

## 3. Phase change in flat-wall channels

In macroscale channels, the boiling process always begins with bubble growth on the channel walls. The two-phase flow transitions along the flow direction into four regimes—bubbly flow (liquid flow carrying vapor bubbles), slug/plug flow (liquid flow with coalesced bubbles), annular flow (a fast-moving vapor core wrapped by a thin, slowly-moving liquid layer), and mist flow (a mixture of vapor and tiny liquid droplets moving at the same speed) [15]. Among all the two-phase flow regimes, annular flow has the highest heat transfer coefficients due to thin film evaporation [15]. In flat-wall silicon microchannels, we observed two different nucleation mechanisms in channels larger than 100 μm and smaller than 50 μm in hydraulic diameter. The two-phase flow directly develops into annular flow or mist flow regime, without a clear transition from bubbly or slug/plug flows. Annular flows in microchannels also achieve higher heat transfer rates than other flow regimes.

### 3.1. Phase change visualization

Using a SONY 2735 CCD camera with controlled shutter speed, we recorded the nucleation process in channels with various hydraulic diameters. In all of these channels, bubbly and slug/plug flow regimes are absent, because a single bubble can quickly grow to the size of the channel diameter and suppress the two regimes.

Table 1
Device structural dimensions

| Structure | Dimension |
|---|---|
| Chip | 6.5 cm long, 2 cm wide, silicon substrate 480 μm thick, glass slide 520 μm thick |
| Beam | 2 cm long, 2 mm wide |
| Reservoirs | 1 cm long, 600 μm wide, 250 μm deep |
| Channels | 10–150 μm wide, 10–200 μm deep, 2 cm long |
| Temperature sensor (back side) | 150 μm long, 110 μm wide, 1 μm junction depth, 8 kΩ resistance |
| Heater (back side) | 2 cm long, 50 μm wide (10 lines), 2 μm thick, 50 Ω resistance |

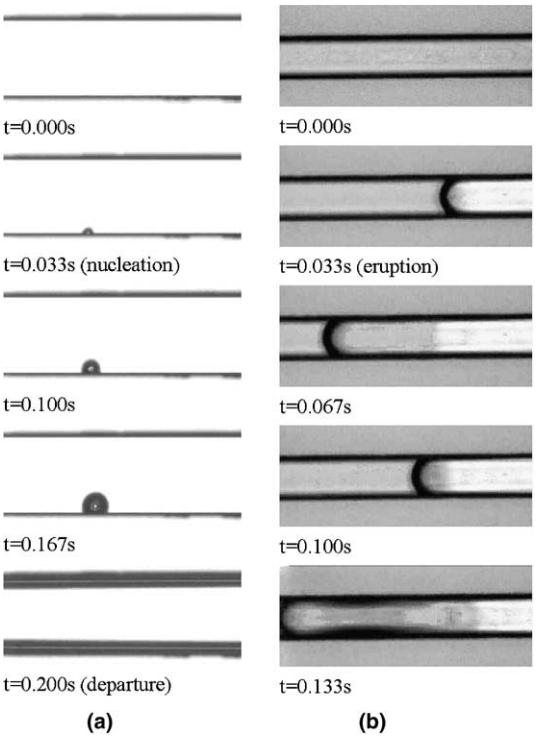


Fig. 3. Bubble nucleation mechanisms and two-phase flow regimes. (a) Bubble nucleation in a 250 μm wide, 130 μm deep (171 μm hydraulic diameter) channel, with 0.5 ml/min DI water flow rate, 94–96 °C wall temperature; (b) Vapor eruption in a 50 μm wide, 40 μm deep (44 μm hydraulic diameter) channel, with 0.02 ml/min DI water flow rate, 120 °C wall temperature.

We also observed two distinct bubble nucleation mechanisms—typical nucleation and eruption boiling. In Fig. 3a, a bubble forms and departs in 0.2 s in a 171 μm diameter channel as a typical nucleation process. The bubble becomes a transient annular flow upon departure, and a steady annular flow develops when more bubbles are departing. In a 44 μm diameter channel shown in Fig. 3b, eruption boiling occurs with no detectable bubble nucleation period. The vapor eruption process completes within 0.033 s, and two-phase flow appears as a single-phase liquid and a two-phase mist separated by a fast oscillating interface in the longitudinal direction. The two nucleation mechanisms are representative for larger than 100 μm diameter (typical nucleation) and smaller than 50 μm diameter (eruption boiling) channels respectively. Channels with 50–100 μm diameters exhibit transitional behaviors, showing both typical nucleation and eruption mechanisms.

### 3.2. Wall temperature measurement

The nucleation mechanism further determines the two-phase flow regime in the microchannel as well as the amount of wall superheat. In our experiment, the flow rates are selected so that the global pressure drop is less than 35 kPa, and the saturation temperature of water is calculated from the measured pressure drop just before the onset of boiling.

With typical bubble nucleation in larger channels, the annular flow eventually develops with a measurably higher heat transfer rate. Fig. 4 shows the wall temperature and global pressure measurement with increasing input heat rate in a 113 μm diameter channel. The wall temperature increases linearly with increasing heat rate in the single-phase region. Typical bubble nucleation is recorded with less than 5 °C wall superheat. A steady annular flow then develops, resulting in a long temperature plateau in the two-phase region. Between the single-phase and two-phase regions, a secondary plateau appears due to liquid out-gassing. While bubbles are seen in out-gassing period, the global pressure drop does not increase because phase change is not involved. The onset of boiling in the plot is defined as the point when a sharp increase in global pressure drop is recorded. The heat loss in this experiment was approximately 42%, estimated from a thermal resistance model for the experimental system [14]. Subtracting the heat loss, the thermal resistances are 95.2 °C/W in the single-phase region and 15.6 °C/W in the fully developed two-phase region. Therefore, the heat transfer rate increases about 5 times due to the two-phase annular flow.

In less than 50 μm diameter channels, where eruption boiling happens, mist flow usually develops and there is no apparent temperature plateau in the two-phase region. Fig. 5 is the wall temperature and global pressure measurement with increasing input heat rate in the 44 μm channel shown in Fig. 3b. In the single-phase region, the wall temperature also increases linearly with

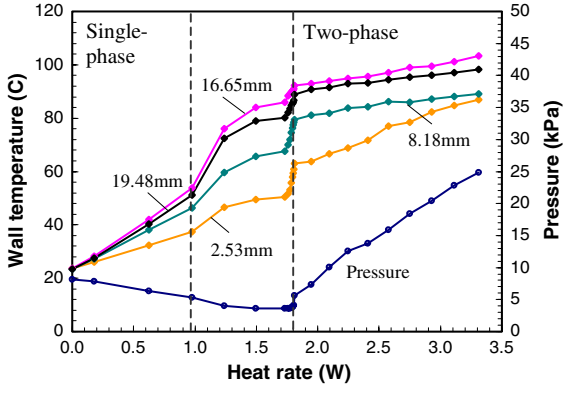


Fig. 4. Wall temperature change from four temperature sensors and global pressure drop as a function of input heat rate in a 100 μm wide, 130 μm deep (113 μm hydraulic diameter) channel at 0.1 ml/min DI water flow rate. The numbers represent the distance between the sensor and the entrance of the microchannel.

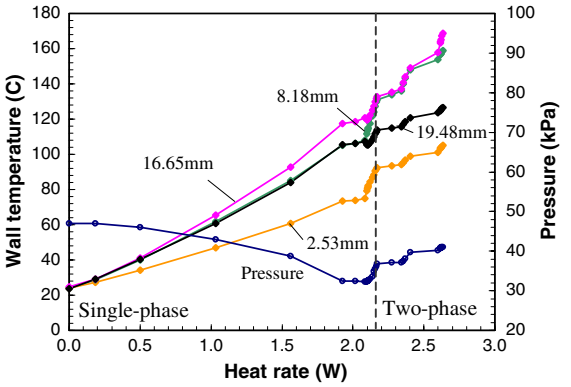


Fig. 5. Wall temperature change from four temperature sensors and global pressure drop as a function of input heat rate in a 50 μm wide, 40 μm deep (44 μm hydraulic diameter) channel at 0.02 ml/min DI water flow rate. The numbers represent the distance between the sensor and the entrance of the microchannel. The short "plateaus" are artificial lines between input heat rate points, not measured temperature plateaus.

the heat rate. However, the single-phase region is extended to nearly 120 °C when vapor eruption suddenly occurs. With the same DI water, there is no apparent out-gassing period as in the 113 μm diameter channel. The wall temperature continues to increase with increasing heat rate in the two-phase region. More than 20 °C wall superheat is characteristic to the eruption mechanism. Because of the large amount of superheat, the high wall temperature quickly turns single-phase water flow into a mist or even pure vapor flow in these small-diameter channels. Mist/vapor flows are known to have poor thermal transport properties, and a temperature plateau is usually not expected. With 10% heat loss in the measurement, the thermal resistance in both single- and two-phase regions is approximately 600 °C/W.

### 3.3. Bubble induced pressure fluctuations

Because of the small internal volume of microchannels, individual bubbles can affect important parameters such as local pressure. Fig. 6a shows high-speed time traces of temperature sensor resistances when a constant heat power is applied to a 113 μm diameter channel. When bubbles begin to form, there are noticeable fluctuations in all locations. The fluctuation frequency is always equal to the bubble departing frequency, which has been confirmed from simultaneous video recording. The fluctuations begin with 3–5 Hz frequency, and increase to 30–40 Hz within a few seconds, indicating more bubble generation and the development of a steady annular flow. These signals are found to be transient pressure fluctuations on the order of 69–138 kPa, caused by individual bubbles forming and departing in the channel. Transient pressure fluctuations induced by bubble nucleation are significantly higher than what have been measured in macroscale channels.

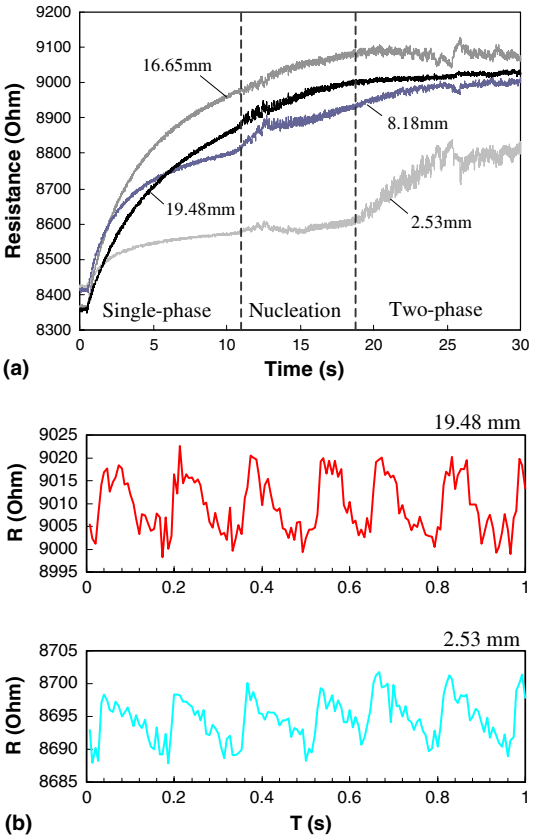


Fig. 6. High speed time traces of the sensor resistance change during the phase change process, showing bubble nucleation induced pressure fluctuations in a 100 μm wide, 130 μm deep (113 μm hydraulic diameter) channel with 0.1 ml/min DI water flow rate. The numbers represent the distance between the sensor and the entrance of the microchannel. (a) Transient resistance change after a constant input heat rate is applied at $t = 0.5$ s. The bubble nucleation begins at $t = 11$ s, and a steady annular flow develops at $t = 18$ s. (b) Highly correlated resistance fluctuations at the inlet and outlet sensor locations when bubbles forming and departing in the channel.

In this experiment, water enters the channel at room temperature, therefore boiling only occurs in the middle of the channel. However, as shown in Fig. 6b, the signal fluctuation is highly correlated along the entire channel, including the entrance of the channel which is under single-phase flow. The fluctuations are determined to be pressure signals rather than temperature signals because only pressure waves are fast enough to cause correlated signals along the length of the channel. Since doped silicon resistors are also sensitive to strain, the temperature sensors can respond to large transient pressure waves. Calibration shows that the sensors have 10 Ω/°C temperature sensitivity and −0.145 to −0.29 Ω/kPa pressure

sensitivity. The two sensitivities function in different frequency domains. Temperature measurements are performed in steady state with less than 1 Hz sampling frequency. With 69 kPa to 1 °C equivalence in the two measurements, the maximum pressure fluctuations only cause about 1–2 °C uncertainty in the steady state temperature. The temperature sensitivity decreases quickly for signals above 1 Hz due to the necessary thermal diffusion time in the system. Therefore, the AC (Alternating Current) signals on top of the DC (Direct Current) temperatures are considered transient pressure components.

## 4. Phase change in enhanced-wall channels

Eruption boiling is not commonly seen in macroscale channels, but has been reported by several research groups in 50–700 μm diameter channels [10,13]. In some previous experiments, this phenomenon has been assumed and/or confirmed to be related to channel dimensions. In this study, we believe that eruption boiling is caused by the lack of active nucleation sites in microchannels. Our further experiments indicate that the boiling mechanism is determined by the wall surface condition rather than the internal space of a microchannel.

### 4.1. Hypotheses

One existing hypothesis about the eruption boiling is that a vapor bubble must overcome extra pressure imposed by channel walls, and bubble nucleation will be suppressed if the internal space of a microchannel is smaller than an "evaporating space" [16]. Using Clausius–Clapeyron equation and a correction factor for the space induced pressure, Peng et al. [16] suggested that the amount of wall superheat $\Delta T_{\text{sup}}$ in a microchannel is determined by

$$\Delta T_{\text{sup}} = T_{\text{w}} - T_{\text{sat}} \geqslant \frac{4CT_{\text{sat}}(v_{\text{v}} - v_{\text{l}})\sigma}{h_{fg}D_{\text{H}}} \tag{1}$$

where $C$ is an empirical constant which is proposed to be approximately 280 on the basis of earlier experiments. This equation also indicates that the degree of wall superheat is an exclusive function of surface tension $\sigma$ with a given channel dimension and the type of liquid.

On the other hand, in the flat-wall silicon channels, we found that bubbles only grew on the side walls, and never on the bottom of the channel. It is known that the DRIE process creates rough side walls to achieve a highly anisotropic etch. Therefore we postulate that the eruption boiling is caused by the wall surface condition. In traditional pool boiling theories, the wall surface condition plays a key role in heterogeneous nucleation because gas-trapping cavities first become nucleation sites and help initiate the phase change. Hsu's model introduces the concept of waiting period, the time required for the liquid to be heated to a higher temperature than that of a bubble embryo, so that the bubble can absorb the heat from surrounding liquid and continue to grow [17]. Only the cavities with a finite waiting period, referred to as effective sites, can potentially become active nucleation sites. He further provided the relationship between the wall superheat and the size range ($r_{\text{c,max}}, r_{\text{c,min}}$) of effective sites:

$$r_{\text{c,max}}, r_{\text{c,min}} = \frac{\delta}{2C_1}\left[1 - \frac{T_{\text{sat}} - T_\infty}{T_{\text{w}} - T_\infty} \pm \sqrt{\left(1 - \frac{T_{\text{sat}} - T_\infty}{T_{\text{w}} - T_\infty}\right)^2 - \frac{8\sigma T_{\text{sat}} v_{\text{v}} C_3}{h_{fg}\delta\Delta(T_{\text{w}} - T_\infty)}}\right] \tag{2}$$

where $C_1$ and $C_3$ are constants related to the shape of the cavity and the contact angle of the bubble embryo. For simplicity, Hsu [17] assumes the bubble embryo has the same diameter as the cavity mouth, and obtains the values as 2 and 1.6 respectively. Eq. (2) indicates that with a given type of liquid and wall superheat, only a given range of nucleation sites can be activated. Therefore, given the cavity sizes in a microchannel, the amount of wall superheat must satisfy the equation in order to initiate the phase change.

Experiments were designed to compare the two hypotheses. We used surfactant to reduce the liquid surface tension to study whether the wall superheat can be

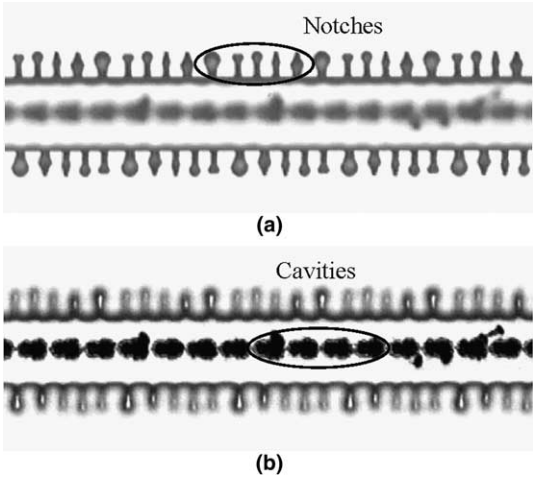


Fig. 7. The notches in the side walls and the cavities in the bottom as surface enhancement. They are designed to trap air to facilitate nucleation process during the phase change. (a) Notches with 4 m opening, 20 μm depth into the side walls. (b) 4–8 μm diameter, 150–250 μm deep cavities in the bottom of the channel.

reduced accordingly. We also fabricated enhanced-wall devices with 4–8 μm notches and cavities defined in channel walls, as shown in Fig. 7. The experiments focus on the boiling mechanism and the wall superheat in channels with less than 100 μm hydraulic diameters.

### 4.2. Phase change visualization

We first added surfactant into water (Triton X-100, 200–10,000 ppm weight concentration) to reduce the liquid surface tension and repeated the phase change experiment in the 44 μm diameter channel shown in Fig. 3b. However, the same type of eruption boiling was observed.

We then conducted phase change experiments in four enhanced-wall channels with 28, 47, 61, and 72.5 μm hydraulic diameters. In all four channels, we observed typical nucleate boiling and confirmed that the cavities induced bubble nucleation. Also the increased density of nucleation sites help to induce a steady annular flow. Fig. 8a shows bubbles generating and departing from the cavities in the bottom of the channel. The sequence of images in Fig. 8b shows a steady annular flow with varying liquid film thickness.

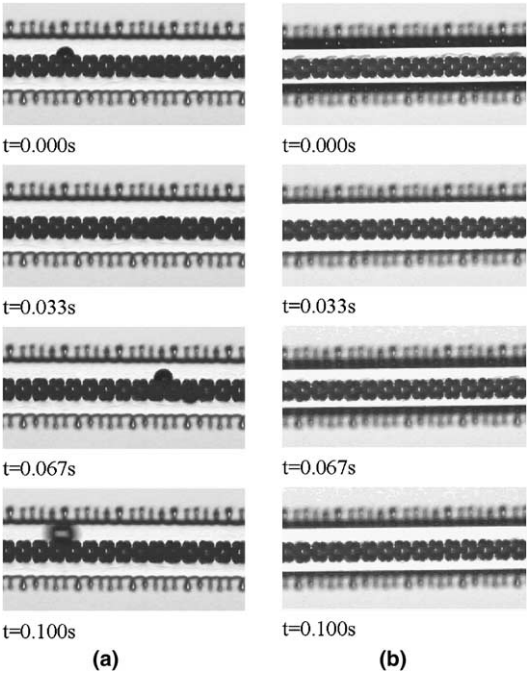


Fig. 8. Bubble nucleation and annular flow patterns in a 120 μm wide, 52 μm deep (72.5 μm hydraulic diameter), enhanced-wall channel. (a) Bubble nucleation from cavities in the bottom of the channel. (b) Annular flow in the channel with varying liquid film thickness.

### 4.3. Wall temperature measurement

Fig. 9 shows the repeated wall temperature measurement in the 44 μm channel with low-surface tension DI water. The trend and shape of the curves are very similar to those in Fig. 5, measured with regular DI water. We estimate the surface tension by taking pictures of a liquid drop on a silicon surface and measuring the contact angle. Estimation shows that the DI water surface tension is reduced by approximately 30% in the 200 ppm Triton X-100 solution. However, vapor eruption occurred in both experiments with more than 20 °C wall superheat without apparent reduction for the low-surface tension liquid. Repeated experiments in a few small-diameter channels with different flow rates yielded the same result. According to Eq. (1), the amount of wall superheat is proportional to the liquid surface tension when the channel size is fixed. Therefore eruption boiling in our experiments is not directly caused by liquid surface tension.

In the phase change experiments with enhanced-wall channels, wall temperature measurement indicates that bubble nucleation occurred with less than 5 °C wall superheat, as shown in the wall temperature plots in Figs. 10 and 11. When the annular flow is induced in the 72.5 μm diameter channel shown in Fig. 10, a temperature plateau is measured, similar as in Fig. 4. Considering approximately 40% heat loss, here the thermal resistance reduces from 105 °C/W in the single-phase region to 22 °C/W in the two-phase region. We also found that in less than 50 μm diameter channels, bubble nucleation causes strong instabilities even if the wall superheat is significantly reduced. As a result, the annular

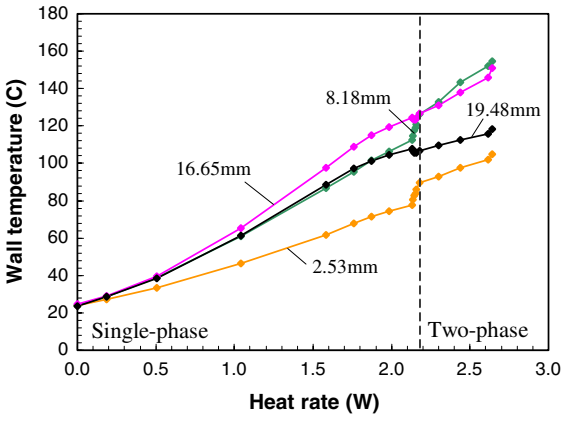


Fig. 9. Wall temperature change from four temperature sensors as a function of heat rate in a 50 μm wide, 40 μm deep (44 μm hydraulic diameter) channel at 0.02 ml/min flow rate of 200 ppm TritonX-100 DI water solution. The numbers represent the distance between the sensor and the entrance of the microchannel.

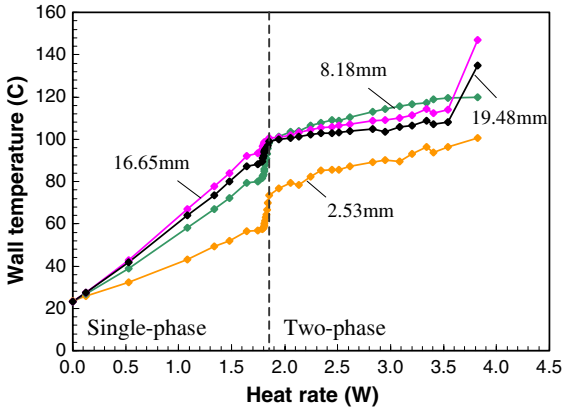


Fig. 10. Wall temperature change from four temperature sensors as a function of the heat rate in a 120 μm wide, 52 m deep (72.5 μm hydraulic diameter) channel at 0.1 ml/min DI water flow rate. The numbers represent the distance between the sensor and the entrance of the microchannel.

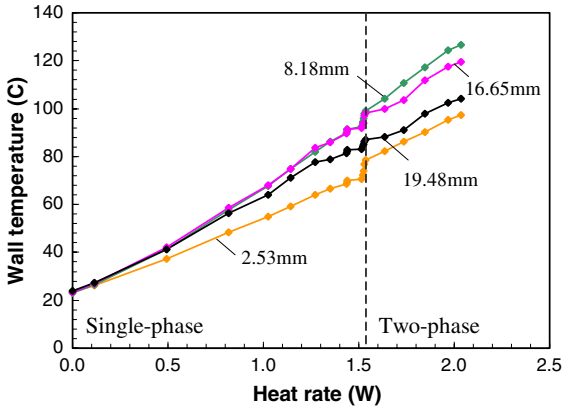


Fig. 11. Wall temperature change from four temperature sensors as a function of the heat rate in a 50 μm wide, 44 m deep (47 μm hydraulic diameter) channel at 0.02 ml/min DI water flow rate. The numbers represent the distance between the sensor and the entrance of the microchannel.

flow changes to the mist flow regime well before anticipated in macroscale channels, which explains the absence of a temperature plateau in Fig. 11.

## 5. Discussion

Table 2 summarizes the experimental parameters of four microchannels discussed in this paper. Microchannel flows usually have much lower flow velocities and Reynolds numbers than those in macroscale channels. Calculation of the Weber number, Capillary number, and Bond number indicates that surface tension is the dominant force in our experiments, although it is not

Table 2
Experimental parameters for representative microchannels

| Parameters | Ch1 | Ch2 | Ch3 | Ch4 |
|---|---|---|---|---|
| Channel dimension (μm × μm) | 100 × 130 | 50 × 40 | 120 × 50 | 50 × 44 |
| Channel wall | Flat | Flat | Enhanced | Enhanced |
| Hydraulic diameter (μm) | 113 | 44 | 72.5 | 47 |
| Mass flow rate (ml/min) | 0.1 | 0.02 | 0.1 | 0.02 |
| Flow velocity (m/s) | 0.128 | 0.167 | 0.278 | 0.152 |
| Reynolds number | 15.4 | 7.9 | 20.8 | 7.5 |
| Weber number | 0.026 | 0.017 | 0.078 | 0.015 |
| Capillary number | 1.68e−3 | 2.19e−3 | 3.65e−3 | 1.99e−3 |
| Bond number | 1.74e−3 | 2.64e−4 | 7.16e−4 | 3.01e−4 |

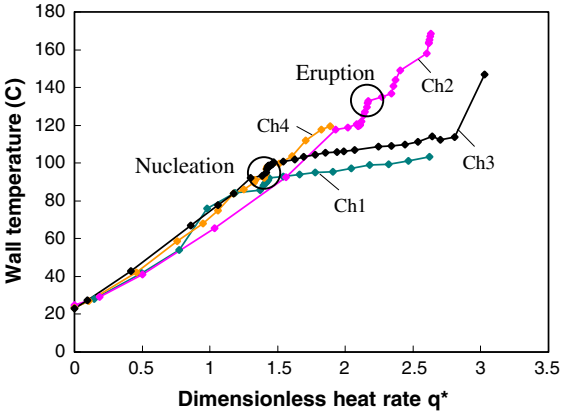


Fig. 12. Wall temperature change as a function of dimensionless heat rate from flat-wall and enhanced-wall channels. Ch1: 113 μm hydraulic diameter, flat-wall channel, 0.1 ml/min DI water flow rate. Ch2: 44 μm hydraulic diameter, flat-wall channel, 0.02 ml/min DI water flow rate. Ch3: 72.5 μm hydraulic diameter, enhanced-wall channel, 0.1 ml/min DI water flow rate. Ch4: 47 μm hydraulic diameter, enhanced-wall channel, 0.02 ml/min DI water flow rate.

proven the primary reason for wall superheat in eruption boiling. Wall temperature measurements performed in these channels are compared in Fig. 12. Temperature measurements in the same location (16.65 mm from the entrance of the channel) in all four channels are plotted in one graph with normalized input heat rate to compensate the difference in flow rates. The dimensionless heat rate $q^*$ is defined as

$$q^* = \frac{q}{\dot{m}c_p(T_{sat} - T_0)} \quad (3)$$

where the heat rate $q$ is divided by the sensible heat of a given mass flow rate $\dot{m}$. The sensible heat $\dot{m}c_p(T_{sat} - T_0)$ is the maximum amount of heat that can be absorbed by the liquid before the phase change takes place. The theoretical saturation temperature (boiling point) of DI water under the experimental conditions ranges from 101 to 103 °C. Comparing the four boiling curves, eruption boiling with large amounts of wall superheat is eliminated by adding cavities to the channel walls, and the enhanced surfaces help to establish a steady annular flow regime in larger than 50 μm diameter channels.

The wall temperature measurements qualitatively support that the nucleation sites affect the wall superheat as well as the nucleation mechanism. This theory is also supported by Kandlikar's recent study on the influence of channel hydraulic diameter on flow boiling heat transfer mechanisms [18]. Using Hsu's model, the required wall superheat can be estimated from the cavity size. In microchannels with thermally fully developed flows (test channels have nearly-constant heat flux boundary condition [14], therefore thermally fully developed flow will appear), we use one half of the channel hydraulic diameter as thermal boundary layer thickness ($\delta = D_H/2$), and assume the liquid is saturated ($T_\infty = T_{sat}$). In Fig. 13, four plots are generated for the range of effective nucleation sites (the region within the parabolas) with 1–100 °C wall superheat for a 11 μm, 45 μm, 75 μm, and a 110 μm diameter channel.

In the flat-wall silicon channels, we found that the DRIE process resulted in fine features ranging from 0.1 to 0.4 μm in the side walls, with a few defects on the order of 2–5 μm in larger channels. Assuming 2–5 μm cavity size in a 110 μm channel and 0.1–0.4 μm cavity size in a 45 μm diameter channel, Hsu's model predicts 1.5–3.5 °C and 18–70 °C wall superheat respectively, which is in good agreement with our measurements in Figs. 4 and 5 (also Ch1 and Ch2 in Fig. 12). For the enhanced-wall channels, using 4–8 μm cavity size in a 75 μm and a 45 μm diameter channel, Hsu's model shows 1.5–2 °C and 2.5–3 °C wall superheat respectively, also in very good agreement with the temperature plots in Figs. 10 and 11 (also Ch3 and Ch4 in Fig. 12). In addition, although the bubbles prefer to grow from the side walls in flat-wall channels (Fig. 3a), they move to the bottom of the enhanced-wall channels (Fig. 8a) and are never observed in the side wall notches. These notches are originally designed as a comparison to the cavities. However, because the notches have the same depth as the channel, the actual opening size is tens of microns. From Fig. 13, this size range falls in the ineffective region (sizes with an indefinite waiting period), which well explains the nucleation preference to the bottom cavities.

In summary, our experimental results support the nucleation site hypothesis, and large amounts of wall superheat associated with eruption boiling can still be explained with Hsu's model. Both typical nucleation and eruption boiling are forms of heterogeneous nucleation where vapor forms on a liquid–solid interface, and the amount of wall superheat is primarily determined by the size and number of active nucleation sites. Eruption boiling tends to occur when the wall superheat exceeds 5–10 °C due to fast evaporation in a very limited internal volume. Fig. 14 is a proposed boiling mechanism and regime map for sub-150 μm diameter microchannels with less than 0.5 m/s water flow velocities, based on our experiments with flat- and enhanced-wall channels. Here we assume the condition for eruption boiling is $\Delta T_{sup} \geqslant 10$ °C, also based on our experimental results. Given the channel hydraulic diameter and wall superheat, the range of effective nucleation sizes ($r_{c,min}, r_{c,max}$) can be calculated from Eq. (2), under assumptions $\delta = D_H/2$ and $T_\infty = T_{sat}$. In Fig. 14, the

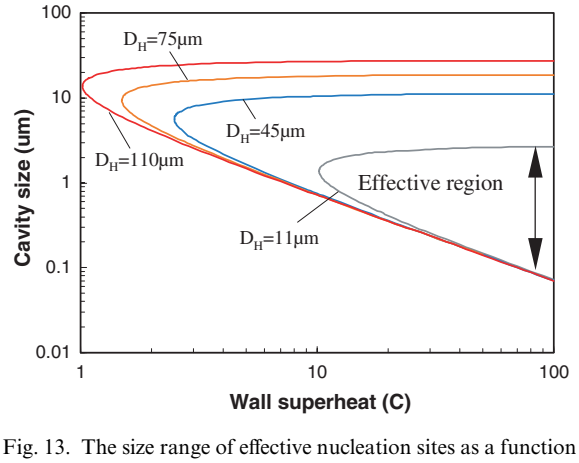


Fig. 13. The size range of effective nucleation sites as a function of wall superheat and channel dimension from Hsu's model.

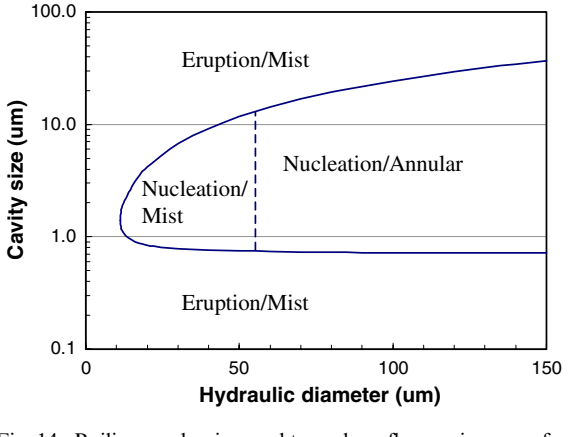


Fig. 14. Boiling mechanism and two-phase flow regime map for sub-150 μm diameter microchannels with less than 0.5 m/s water flow velocity.

calculated $r_{c,min}$ and $r_{c,max}$ are plotted as a function of $D_H$. The region within the parabola defines the microchannels where typical nucleation tends to occur ($\Delta T_{it\ sup} < 10$ °C). The area is further divided into mist flow and annular flow regions according to our observation that mist flow tends to dominant in less than 50 μm diameter channels. In microchannels outside of the parabola region, eruption tends to occur and mist flow is the only dominant flow regime as the result of eruption boiling.

The "evaporating space" hypothesis was not verified in our experiments, and we believe this theory may apply to ideally smooth channel walls, or below a certain size threshold in microchannels. The "evaporating space" hypothesis assumes the internal space of the channel as a single nucleation site, while we treat the defects or cavities in the channel walls as nucleation sites. As shown in Fig. 13, the minimum amount of wall superheat is a function of the thermal boundary layer thickness (channel diameter), and the actual wall superheat is primarily determined by the cavity size. For example, for channels larger than 11 μm in diameter, the wall superheat can be reduced to less than 10 °C by creating appropriate cavities in the channel wall. However, for channels smaller than 11 μm in diameter, the minimum amount of wall superheat will be 10 °C regardless of cavity sizes and eruption boiling may become the only mechanism for phase change. We expect an interesting transition in boiling phenomena in less than 11 μm diameter channels.

## 6. Conclusions

We found that two-phase forced convective theories are valid down to 27 μm diameter silicon microchannels, including both heat transfer [14] and flow behavior. However, due to the scaling of the channel dimensions, factors that can be neglected in macroscale channels become dominant, such as the condition of individual nucleation sites as well as the formation of individual bubbles. This effect, although not a violation of two-phase theories, leads to some unique phenomena in two-phase flows in microchannels. First, bubbly and slug flows that exist in macroscale channels are often absent in microchannels. This is beneficial to microchannel heat sinks because the desired annular flow pattern can be quickly established. Second, vapor bubbles can cause 69–138 kPa transient pressure pulses at the onset of boiling. These pressure pulses may damage the device, and are expected to affect local boiling point and equilibrium conditions. Third, the phase change mechanism (typical nucleation and eruption boiling) is closely associated with wall surface conditions, and the two-phase flow regime has a strong dependence on the phase change mechanism. In order to induce and maintain a steady annular flow for microchannel heat sink applications, the channel wall must have enough gas-trapping cavities to ensure typical nucleation. Fourth, the mist flow tends to dominate in sub-50 μm diameter channels even with wall surface enhancements. The phase change mechanism and regime map in Fig. 14 provides a reference for design of microchannel heat sinks. These findings will help to better understand the flow behavior in microchannels, and a new generation of heat sinks for microprocessors may be expected in the near future.

## Acknowledgments

The work was supported by DARPA HERETIC program under DARPA Contract F33615-99-C-1442, Stanford Graduate Fellowships (Lian Zhang), and National Defense Science and Engineering Graduate Fellowship (Evelyn N. Wang). The devices were fabricated at Stanford Nanofabrication Facility, funded by the National Science Foundation under award number ECS-9731294. We thank Prof. Juan Santiago at Stanford University and James Maveety at Intel Corporation for their valuable discussions, and Shilajeet Benerjee for his assistance in building the experimental system.

## References

[1] G.E. Moore, Cramming more components onto integrated circuits, Proc. IEEE 86 (1) (1998) 82–85, reprinted from Electronics 38 (8) (1965) 114–117.
[2] Intel microprocessor quick reference guide, http://www.intel.com/pressroom/kits/quickreffam.htm.
[3] International Technology Roadmap for Semiconductors 2003 update, http://public.itrs.net/Files/2003ITRS/Home2003.htm.
[4] D.B. Tuckerman, R.F.W. Pease, High-performance heat sinking for VLSI, IEEE Electron Dev. Lett. EDL 2 (5) (1981) 126–129.
[5] C.D. Patel, Enabling pumped liquid loop cooling: justification and the key technology and cost barriers, in: Proceedings of International Conference on High-Density Interconnect and Systems Packaging, IMAPS, Reston, VA, 2000, pp. 145–152.
[6] L. Jiang, J. Mikkelsen, J.-M. Koo, D. Huber, S. Yao, L. Zhang, P. Zhou, J.G. Maveety, R. Prasher, J.G. Santiago, T.W. Kenny, K.E. Goodson, Closed-loop electroosmotic microchannel cooling system for VLSI circuits, IEEE Trans. Components Packaging Technol. 25 (3) (2002) 347–355.
[7] S. Zeng, C.-H. Chen, J.C. Mikkelsen, J.G. Santiago, Fabrication and characterization of electrokinetic micro pumps, in: Proceedings of ASME ITHERM, IEEE, Piscataway, NJ, 2000, pp. 31–36.
[8] L. Jiang, M. Wong, Y. Zohar, Phase change in microchannel heat sink under forced convection boiling,

in: Proceedings of IEEE MEMS Workshop, IEEE, Piscataway, NJ, 2000, pp. 397–402.

[9] M.E. Steinke, S.G. Kandlikar, Flow boiling and pressure drop in parallel flow microchannels, in: 1st International Conference on Microchannels and Minichannels, ASME, New York, NY, 2003, pp. 567–579.

[10] X.F. Peng, B.X. Wang, Forced convection and flow boiling heat transfer for liquid flowing through microchannels, Int. J. Heat Mass Transfer 36 (14) (1993) 3421–3427.

[11] D.B.R. Kenning, Y. Yan, Saturated flow boiling of water in a narrow channel: experimental investigation of local phenomena, IChemE Transactions A, Chem. Eng. Res. Des. 79 (A4) (2001) 425–436.

[12] Y.P. Peles, L.P. Yarin, G. Hetsroni, Evaporating two-phase flow mechanism in micro-channels, Proc. SPIE 3680 (1999) 226–229.

[13] Y. Peles, Two-phase boiling flow in microchannels-instabilities issues and flow regime mapping, in: 1st International Conference on Microchannels and Minichannels, ASME, New York, NY, 2003, pp. 559–566.

[14] L. Zhang, J.-M. Koo, L. Jiang, M. Asheghi, K.E. Goodson, J.G. Santiago, T.W. Kenny, Measurements and modeling of two-phase flow in microchannels with nearly-constant heat flux boundary conditions, J. MEMS 11 (1) (2002) 12–19.

[15] V. Carey, Liquid–Vapor Phase-Change Phenomena, Hemisphere Publishing Corporation, Washington DC, 1992, pp. 483–485.

[16] X.F. Peng, H.Y. Hu, B.X. Wang, Boiling nucleation during liquid flow in microchannels, Int. J. Heat Mass Transfer 41 (1) (1998) 101–106.

[17] Y.Y. Hsu, On the size range of active nucleation cavities on a heating surface, ASME J. Heat Transfer (Aug.) (1962) 207–216.

[18] S.G. Kandlikar, Heat transfer mechanisms during flow boiling in microchannels, J. Heat Transfer 126 (2004) 8–16.